AIAA JOURNAL
Vol. 34, No. 9, September 1996

Sound Propagation and Radiation in a Curved Duct

P. Malbéqui* and C. Glandier*
ONERA, 92322 Châtillon Cedex, France
and
C. Reynier†
Institut National des Sciences Appliquées de Rouen, 76131 Mont-St-Aignan Cedex, France

An investigation of sound propagation and radiation in a curved duct using a boundary integral method is presented. The duct of interest is assumed to be hard walled both inside and outside. To avoid interference between the fields radiated from both of its ends, the straight part of the duct is closed with a rigid disk. The acoustic source placed close to this disk simulates a spinning mode. Experiments were also carried out in an anechoic chamber for an identical duct geometry. Comparisons between numerical and experimental results are in good agreement. The modal analysis shows, in particular, that all propagating modes are present at the curved end, for a single pure mode at the source. This result is in agreement with previous analytical studies, which established that several angular modes are required to satisfy the Helmholtz equation in the curved part of the duct. As a result of this modal redistribution, the directivity patterns are not axisymmetrical around the duct exit centerline.

Nomenclature

c	= ambient speed of sound
d	= characteristic size of the mesh elements
f	= frequency
$f_{\text{cutoff}}(m, n)$	= cutoff frequency for mode (m, n)
G	= free-field Green's function
J_m	= mth order Bessel function of the first kind
J'_m	= first-order derivative of J_m
k	= total wave number
m	= azimuthal mode number
n	= radial mode number
p	= acoustic pressure
R	= duct radius
$\boldsymbol{r}_M$	= coordinate vector of the observation point M
$\boldsymbol{r}_P$	= coordinate vector of a point P belonging to the mesh
(r, θ, ϕ)	= spherical coordinate system
S_1	= source surface
S_2	= duct surface
λ	= acoustic wavelength
μ	= double-layer potential
(ρ, α)	= cylindrical coordinate system; see Fig. 1
σ	= single-layer potential
χ_{mn}	= nth zero of J'_m
ω	= angular frequency $(2\pi f)$

I. Introduction

MOST analytical solutions to sound propagation and radiation problems in ducts are based on the standard Tyler and Sofrin model.[1] This theory gives a good insight into the physical phenomenon, but in practice, its applications are restricted to straight semi-infinite baffled cylindrical ducts. Moreover, this type of analytical solution is not suited to the evaluation of sound attenuation by an acoustic lining of finite length placed on the duct wall. More recently, numerical methods for predicting sound radiation in more realistic duct configurations have been developed. These numerical techniques fall into two categories: 1) finite difference and finite element methods (FEM) and 2) boundary integral methods (BIM).

The first class of methods is generally used for analyzing sound propagation in ducts in the presence of a mean flow. The numerical solution is limited to low frequencies and short ducts because of the large number of grid points required to resolve the axial wavelength of the acoustic wave. The number of grid points is proportional to the frequency and duct length, and inversely proportional to one minus the Mach number. Some progress has been achieved for the study of propagating modes (see, for instance, Baumeister[2]); the use of a time-dependent finite difference scheme reduces drastically the storage and CPU requirements.

However, some attention must be given to the description of the exit impedance. One of the main difficulties arising in finite difference techniques is the introduction of the correct boundary condition at the duct exit because this condition, usually described as a wave impedance, depends on the solution itself. The admittance function suggested by Baumeister[2] corresponds to a plane wave impedance. This implies that only one mode is incident on the boundary or that the admittance function is independent of the modal composition. In addition, this numerical scheme does not converge for evanescent modes. Extending the duct length to prevent transient reflections solves the stability problem at a significant cost in terms of computational efficiency.[3] Cabelli[4] reframed these boundary conditions to simulate an anechoic termination for a multiplicity of modes and to allow reflections at the source location. The anechoic termination assumption is a powerful tool for studying propagation in ducts, but it may lead to an overestimation of the radiated field. Thus, it is not valid for duct configurations with strong reflections at their ends. Moreover, in the presence of a mean flow of nonnegligible Mach number, the exit impedance may be different from the assumed impedance.

Another drawback of finite difference techniques comes from the heavy computation time and storage capacity requirement for computing the acoustic pressure in the midfield and in the far field, since a very large number of grid points is needed to mesh the fluid.

A recent paper by Roy and Eversman[5] presents an attractive method for improved finite element modeling of the radiation problem. The proposed method combines conventional FEM in the near field and a wave envelope method in the far field. The envelope elements are built to ensure the far field decays with the inverse of the distance from the duct exit.

BIMs are an interesting alternative. They are based on an integral representation of the sound field. The integral equations are solved only at the boundaries (i.e., the duct surface and the source plane), so that the number of nodes for surface meshes is much smaller than for three-dimensional finite difference volume meshes. Another important advantage of BIM is that they take the Sommerfeld's radiation condition automatically into account. As discussed, this

Presented as Paper 93-4376 at the AIAA 15th Aeroacoustics Conference, Long Beach, CA, Oct. 25–27, 1993; received Jan. 11, 1995; revision received April 17, 1996; accepted for publication April 18, 1996.

*Engineer, Department of Physics, Division of Acoustics, B.P. 72.
†Graduate Student, Department of Mathematics, B.P. 8.

condition can only be approximated in finite difference techniques. However, the free-field Green's function is required in the integral formulation, so that solutions can be obtained only in homogeneous media or in the presence of a uniform mean flow. In practice, this latter limitation reduces the application of the method: for instance, BIMs are not suited to the analysis of sound propagation in ducted fans in the presence of a strongly nonuniform mean flow profile.

A FEM/BIM coupled approach can combine the advantages of the FEM and BIM. The FEM is used for the in-duct propagation in the presence of mean flow with reduced computer storage and CPU time. The BIM can be used to predict the pressure radiated outside the duct.

Geometrical acoustics is another approach to handle the sound propagation and radiation problem. Ray theory can predict propagation in a lined duct with a realistic geometry in the presence of a mean flow. This technique has been applied by Kempton,[6] Kempton and Smith,[7] and Boyd et al.[8] for the propagation of broadband fan noise. Geometrical acoustics is a high-frequency approximation, and the ray solution is independent of the frequency. As a limitation, the ray theory is only appropriate if the frequency is far from the duct cutoff frequency.

Our application concerns acoustic radiation from helicopter turboshaft engine inlets. The curved duct studied represents a simplified model of an engine inlet. If the Mach number in the engine inlet is small, then the BIM is appropriate for this type of problem. The numerical calculations were performed using a BIM originally developed by Hamdi.[9] The BIM is formulated in the frequency domain. An excessive CPU time would be required for broadband noise where a sweep in frequency is necessary. However, this formulation is well suited to the present application of the discrete frequency noise generated by the compressor of the engine. The code has already been validated at ONERA in previous studies for scattering applications[10,11] and for radiation from straight circular or annular ducts.[12] Hamdi and Ville[13] presented an application of the method to sound radiation from a straight open duct. Comparisons with experimental results validated the method for this basic configuration.

Our objective is to demonstrate the capabilities and the interest of the BIM for analyzing sound propagation and radiation in a more complex duct geometry. This paper starts with a brief presentation of the theoretical basis of the BIM (Sec. II). The meshes for the duct are then presented in Sec. III. Section IV describes the experiments carried out in an anechoic chamber, for the same duct geometry. Finally, three types of results are discussed in Sec. V: 1) the azimuthal structure of the wall pressure field at the end of the duct, 2) far-field directivity patterns, and 3) the pressure distribution on the end cross section of the bend. Numerical and experimental results are compared for the first two configurations.

II. Boundary Value Problem for the Curved Duct

General Problem Formulation

This section gives a brief description of the boundary value problem for a curved duct. Let us consider a curved duct defined by the surface S_2, and an acoustic source represented by a pressure distribution on the S_1 disk (Fig. 1). The duct is assumed to be hard walled both inside and out, but the BIM also allows computations in the presence of an absorbing material introduced as an acoustic impedance on the duct walls.

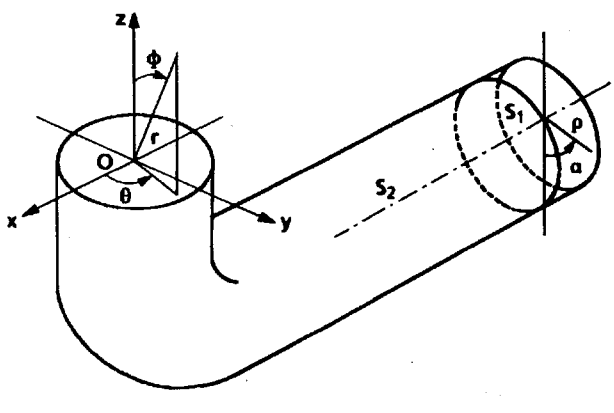

Fig. 1 Problem geometry.

The boundary value problem for the pressure field p is described by the following system:

$$\Delta p + k^2 p = 0 \tag{1}$$

in the fluid

$$\frac{\partial p}{\partial n} = 0 \tag{2}$$

on S_2 and

$$p = A J_m[\chi_{mn}(\rho/R)]e^{-im\alpha} \tag{3}$$

on S_1 with

$$\lim_{r\to\infty} r\left(\frac{\partial p}{\partial r} - ikp\right) = 0 \tag{4}$$

where $k = \omega/c$ is the total wave number (ω is the angular frequency of the acoustic source).

At any point in the fluid, the pressure field is the solution of the Helmholtz equation (1). Equation (2) corresponds to the zero normal acoustic velocity condition on the rigid wall S_2. Equation (3) describes the pressure distribution imposed on the source disk S_1. This definition corresponds to a pure mode in the case of a rigid cylindrical duct. Here χ_{mn} is the nth zero of the derivative of the mth-order Bessel function [$J'm(\chi_{mn}) = 0$]. The amplitude A of the mode is adjusted a posteriori to give the same maximum sound pressure levels (SPL) for the numerical and experimental directivity patterns. At infinity, the pressure field satisfies the Sommerfeld's radiation condition [Eq. (4)].

In BIM, the boundary problem is replaced by equivalent integral relations. Further details on the boundary integral formulation developed by Hamdi can be found in his doctoral thesis.[9] The following integral representation is used:

$$p(\boldsymbol{r}_M) = \int_{S_1} \sigma(\boldsymbol{r}_P) G(\boldsymbol{r}_M, \boldsymbol{r}_P)\, \mathrm{d}S_1 - \int_{S_2} \mu(\boldsymbol{r}_P) \frac{\partial G(\boldsymbol{r}_M, \boldsymbol{r}_P)}{\partial n_P}\, \mathrm{d}S_2 \tag{5}$$

where

$$G(\boldsymbol{r}_M, \boldsymbol{r}_P) = -\frac{1}{4\pi} \frac{\exp(ik|\boldsymbol{r}_M - \boldsymbol{r}_P|)}{|\boldsymbol{r}_M - \boldsymbol{r}_P|} \tag{6}$$

is the free-space Green's function and $\sigma(\boldsymbol{r}_P)$ and $\mu(\boldsymbol{r}_P)$ are a single-layer and a double-layer potential, respectively.

Applying the boundary conditions (2) and (3) leads to a system of integral equations for the potentials σ and μ. These integral equations could be solved using self-collocation techniques. To avoid the computation of the finite part of the double-layer integral equation, a variational formulation is used. As described by Hamdi,[9] the variational formulation avoids the difficulty of handling singular integrals on the source and duct surface. Moreover, the double-layer potential μ is set to zero at the duct inlet to avoid the computation of the integral along the regular contour of the surface S_2. It also physically ensures the pressure jump is zero.

Numerical surface integrals involved in this formulation are computed using Gaussian integration. In the BIM code, the number of Gaussian points is assumed to be the same for the self-influence surface and the cross-influence surface. A convergence study[10] in the case of the scattering of a plane wave by a rigid sphere shows that the error falls below 9% when using three Gaussian points for both self- and cross-influence triangular elements. This ensures the convergence of the BIM, as well as sufficient accuracy for engineering purposes. A complementary analysis[14] indicates that increasing the number of Gaussian points improves the near-field solution very close to the sphere surface but does not improve the far-field solution. For the present curved duct configuration three Gaussian points are used for linear triangular elements and four points for linear quadrilateral panels. The agreement discussed subsequently between numerical and experimental results confirms the convergence of the BIM.

Finally, the potentials are computed in a discrete form using a surface mesh on S_1 and S_2. This leads to a complex symmetrical influence matrix, and σ and μ are then solutions of a linear algebraic system.

Once σ and μ are known on the mesh, the acoustic pressure at any point in the fluid can be obtained from Eq. (5). At points in the direct vicinity of the mesh surface, the numerical surface integral in Eq. (5) becomes singular. This problem has been studied for the situation of scattering by the rigid sphere of radius 1 m (Ref. 14). Numerical tests show that the acoustic pressure is accurately computed on a radius greater than 1.05 m when using a surface mesh with a characteristic size of the elements of the order $\lambda/4$ and three Gaussian points to compute the surface integrals. Note that this drawback does not hold for our application. The pressure field of interest here is the far-field pressure and the pressure on the duct surface for modal analysis.

At points belonging to the surface of the duct, the expression for the pressure is given by

$$p(r_M) = \frac{\mu(r_M)}{2} + \int_{S_1} \sigma(r_P) G(r_M, r_P)\, dS_1 - \int_{S_2} \mu(r_P) \frac{\partial G(r_M, r_P)}{\partial n_P}\, dS_2 \tag{7}$$

Source Modeling

The acoustic source on S_1 [Eq. (3)] represents a spinning mode (m, n) emitted close to the end of the straight duct. Obviously, this source does not model the actual turbine noise; the spinning mode only describes the spatial pressure field generated by the compressor. The source modeling also reproduces the pressure field generated by the acoustic drivers of the experiment. However, in the experimental configuration, the radial mode number n is not fixed a priori and depends on the propagation problem itself.

One disadvantage of this model is that it does not allow one to control the incident pressure field and to separate it from the reflected field. The pressure field imposed on S_1 corresponds to the total pressure field, which is the sum of the incident waves plus the waves reflected by the duct end. A pure (m, n) mode will only be approximated by the experiment if the magnitude of the reflected field is small with respect to the incident field in the vicinity of the source location.

III. Surface Mesh

Figure 2 shows the geometry of the curved duct. The duct surface (S_2) is made up of three parts: 1) a straight duct (D_1) of length 1.8 m and radius $R = 0.15$ m, 2) a torus (T) of internal radius $R_i = 0.09$ m and external radius $R_e = 0.39$ m, and 3) a short duct (D_2) of length 0.1 m and radius $R = 0.15$ m.

For ducts with both ends open, interference between the sound emitted from both inlet and exit will dramatically alter the far-field radiation pattern.[15] To eliminate this phenomenon, the end of the long duct D_1 is closed with a rigid disk.

The acoustic source on the S_1 surface is located close to the end of the D_1 straight duct. A small cavity is thus created between the duct end and the source disk (i.e., a 3.6-cm-long cylinder of radius 15 cm), so that the troublesome irregular frequency problem may arise in the BIM computation. Mébarek and Hamdi[16] developed a technique that overcomes this difficulty. It consists of introducing an absorbing element inside the cavity. However, this problem can be easily avoided here with an appropriate choice of the cavity size. For

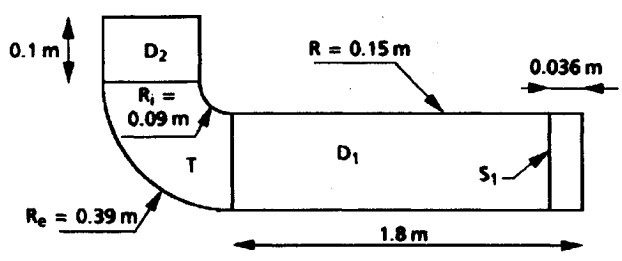

Fig. 2 Curved duct geometry.

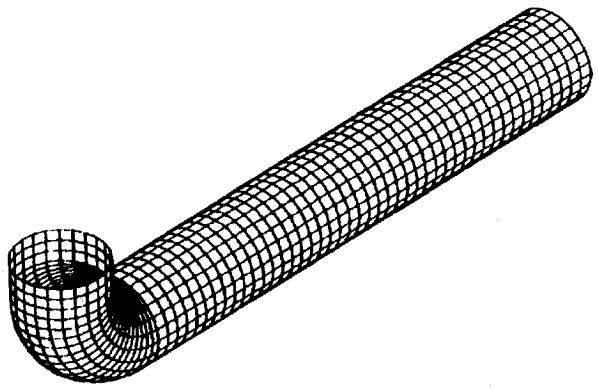

Fig. 3 Surface mesh for the curved duct.

a cylindrical cavity with length l and radius R, the lowest resonance frequency f_r of the cavity is given by $f_r = c/4l$. Taking $l = 3.6$ cm yields $f_r = 2341$ Hz. Because this value is greater than the maximum frequency of the experiment (2 kHz), there is no irregular frequency in the frequency range of interest.

The duct mesh and the source disk mesh were generated using MOSAIC® software. The number of nodes and elements required depends on the acoustic wavelength λ. For engineering purposes, the $d \leq \lambda/4$ criterion, where d is the characteristic size of the elements, ensures convergence of the BIM and yields accurate results.[9,10]

For the present application, the frequency range is 1–2 kHz. According to the $d \leq \lambda/4$ criterion, 1706 nodes and 1704 elements are sufficient for meshing the entire duct surface (see Fig. 3).

IV. Experiments

Experimental Setup

Basic acoustic experiments were carried out at ONERA in an anechoic chamber for studying the influence of duct geometry on sound propagation and radiation.[17] Figure 4 shows the details of the experimental setup. The duct is made of 0.5-cm-thick polyvinylchloride and has the geometry described in Sec. III. To avoid interference effects, absorbing material is placed at the end of the straight duct D_1.

The acoustic source consists of a spinning mode synthesizer placed close to the end of the long duct. This apparatus is made of 12 James B. Lansing 2420 acoustic drivers mounted in one section, on the duct wall, with a 30-deg spacing. Azimuthal modes in the $m = -5$ to $+5$ range can be generated without spatial aliasing. The directivity patterns near the exit are measured by a moving microphone. Two circular arrays of 12 Brüel and Kjaer 0.25-in. microphones of type 4135, located every 30 deg, are mounted on the duct wall, both near the source and near the bend exit. They are used to perform modal analyses of the in-duct acoustic field.

Acoustic Mode Generation

Acoustic drivers can be considered as monopole sources. Our source array makes it possible to impose the azimuthal composition of the incident acoustic field, but, as stated in Sec. II, for a given azimuthal mode m, the radial structure of the field strongly depends on the propagation conditions in the duct. To avoid this drawback, we use the fact that at a given frequency the duct acts as a low-pass filter for radial modes. For a given (m, n) mode, the cutoff frequency (see Table 1) is given by the relation

$$f_{\text{cutoff}}(m, n) = c\chi_{mn}/2\pi R \tag{8}$$

All cases investigated are such that

$$f_{\text{cutoff}}(m, 1) < f < f_{\text{cutoff}}(m, 2) \tag{9}$$

Only the $n = 1$ radial mode can propagate for azimuthal order m at the source, at frequency f. Under these conditions, accurate comparisons between experimental results obtained for various duct configurations, as well as comparisons between experimental and BIM results, are possible.

Table 1 Cutoff frequency for a circular rigid duct of radius R = 0.15 m, according to Eq. (8)

$\|m\|$	$f_{\text{cutoff}}(m, 1)$	$f_{\text{cutoff}}(m, 2)$
0	0	—
1	664	1923
2	1101	2419
3	1515	2891
4	1918	3348

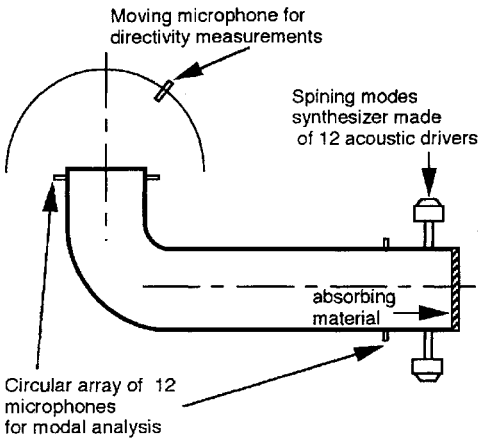

Fig. 4 Experimental setup for studying the acoustic behavior of a curved duct.

V. Results

Modal Analysis

The modal decomposition is obtained by taking the Fourier transform of the wall pressure field with respect to the azimuth angle.

In the experimental case, the modal analysis is performed on the pressure measured by the 12 microphone array, using a method developed to improve the signal to noise ratio.[18]

Similarly, for the BIM, the acoustic pressure is computed on an annular surface at the bend exit (this surface is shaded in Fig. 5). The pressure field on this surface is evaluated at the Gaussian points of the elements using Eq. (7).

Figures 6a and 6b correspond to results obtained at 1 kHz for a pure mode at the source, with azimuthal orders $m = 0$ and 1, respectively. For a pure azimuthal mode at the source, the modal analysis reveals that all propagating modes are present at the curved exit. For instance, in the $m = 0$ source configuration, the $m = -1$ and $m = 1$ components are generated. The additional modes are the result of modal conversion occurring on the bend. In contrast, for the case of a straight cylindrical duct, a given mode is detected at the exit only if it is present at the source location.

For higher frequencies, the number of modes increases (see Figs. 7 and 8). For instance, at $f = 2$ kHz, all propagating modes between $m = -4$ and $m = 4$ are present, as expected from the cutoff relation (8).

Note from Figs. 6–8 that comparisons between experimental and numerical results show a good agreement. In the 1–2-kHz range, the modal redistribution toward all propagating modes is well retrieved using the BIM. Figures 6 and 7 also show that higher nonpropagating modes are present in the experimental results, probably because of background measurement noise. Nevertheless, their levels are very low, about 30–40 dB below the levels of the propagating modes. These modes are obviously not predicted by the computation.

Far-Field Directivity Patterns

Far-field directivity patterns are presented in Figs. 9–15. The experimental and computed SPL are plotted in two planes perpendicular to the duct exit plane: 1) in the $\theta = 90$-deg plane, for $-90 \leq \phi <= 90$ deg and 2) in the $\theta = 0$ plane, which corresponds to the duct symmetry plane, for $0 \leq \phi \leq 90$ deg. The distance r from the center of the exit section to the observation point is 1.4 m.

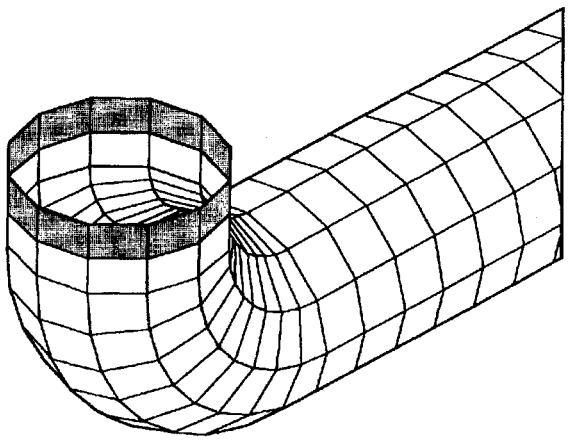

Fig. 5 Annular surface at the exit of the duct mesh used for the modal analysis.

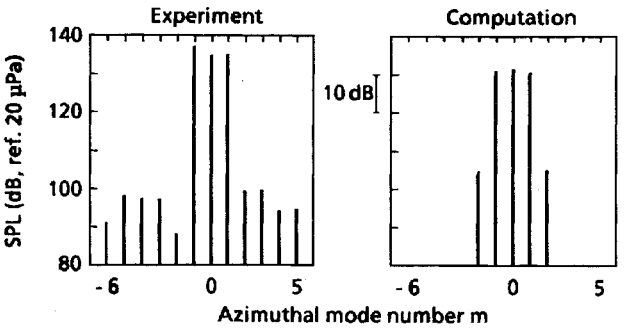

a) $m = 0$ at the source

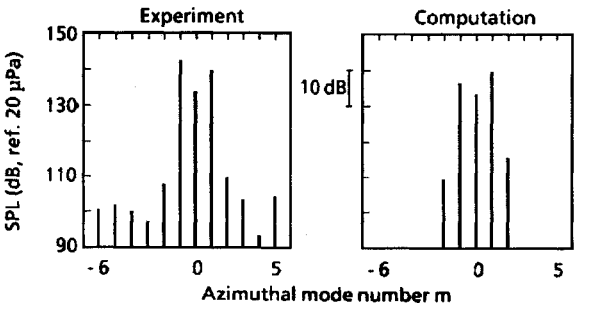

b) $m = 1$ at the source

Fig. 6 Modal analysis of the wall pressure field at the duct exit, at f = 1 kHz.

$\theta = 90$-deg Plane

At 1 kHz, for $m = 0$ (Fig. 9), the directivity pattern exhibits a perfectly symmetrical lobe. For $m = 1$ (Figs. 10 and 11), the pattern is no longer symmetrical. As Lévy[19] pointed out, this result can be explained by phase differences between the various azimuthal components at the bend exit. Lévy[19] used the Tyler and Sofrin model to compute directivity patterns with measured azimuthal components from the earlier described experiment as input data. He showed that adding coherently all modal contributions leads to a close agreement with experimental directivity patterns. In both cases the computational and experimental results are in good agreement.

At $f = 1.5$ kHz, for $m = 2$, differences appear between numerical and experimental results in the $\phi = 10$–90 deg region (Fig. 12). The modal analysis near the source presented in Fig. 7b reveals that the pressure field reflected by the bend contains several propagating modes. In particular, the contribution of the $m = 3$ component is of the same order of magnitude as the contribution of the $m = 2$ source mode. This makes the computational assumption of a pure mode at the source no longer valid and might explain the differences.

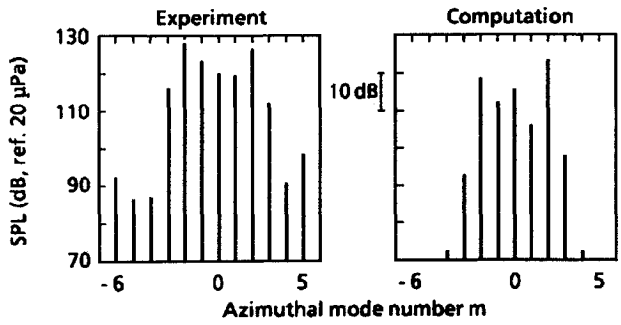

a) $m = 1$ at the source

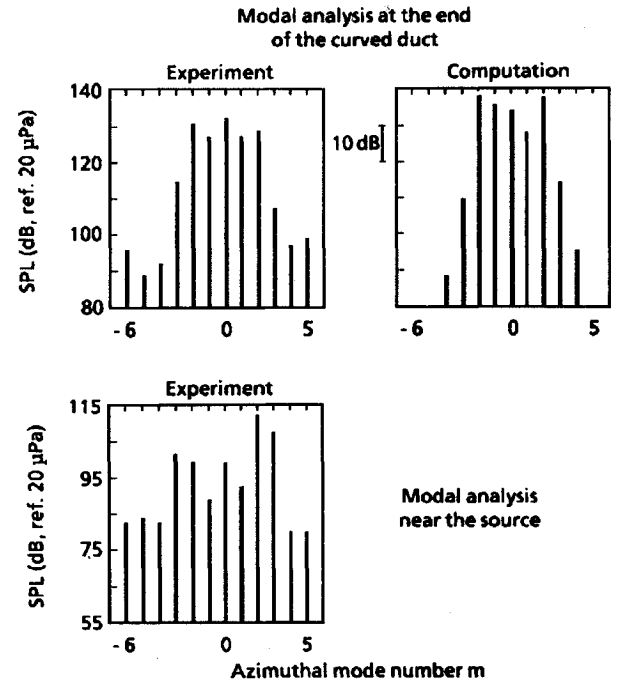

b) $m = 2$ at the source

Fig. 7 Modal analysis of the wall pressure field at the duct exit, at f = 1.5 kHz.

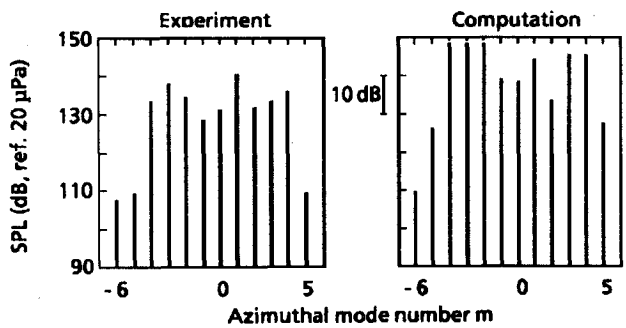

Fig. 8 Modal analysis of the wall pressure field at the duct exit, at f = 2 kHz, for $m = 2$ at the source.

θ = 0-deg Plane

At 1 kHz, for the plane wave mode ($m = 0$) at the source, a significant directionality is observed in Fig. 13. The main lobe extends from ϕ = 0–30 deg. For the $m = 1$ configuration (Fig. 14), the SPL on the duct axis (near $\phi = 0$) is nonnegligible. Remember that this value is zero for $m = 1$ in a straight duct. This result is explained by the contribution of the $m = 0$ component resulting from the propagation in the bend (see Fig. 6b). In these two cases, the agreement between theory and experiment is very good.

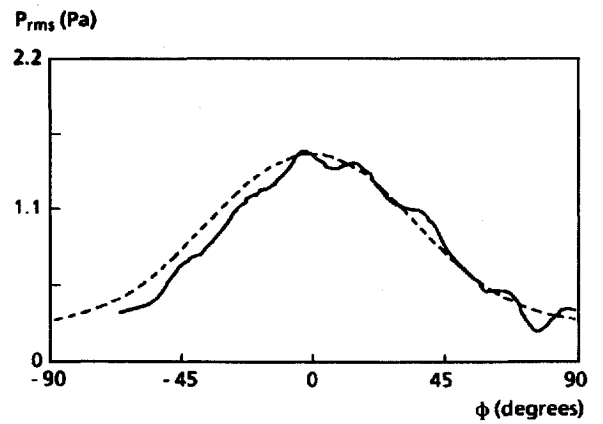

Fig. 9 Far-field directivity pattern in the θ = 90-deg plane, f = 1 kHz, azimuthal mode m = 0: - - - -, computation and ——, experiment.

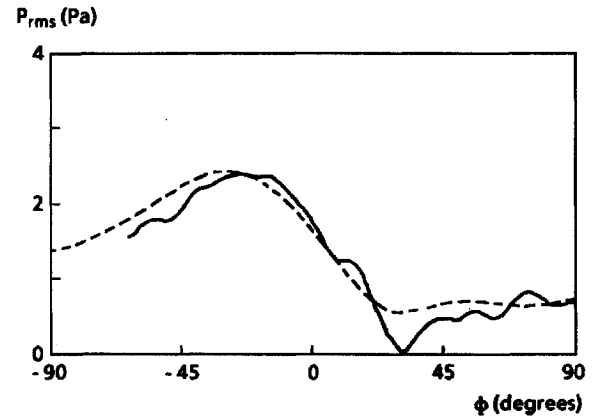

Fig. 10 Far-field directivity pattern in the θ = 90-deg plane, f = 1 kHz, azimuthal mode m = 1: - - - -, computation and ——, experiment.

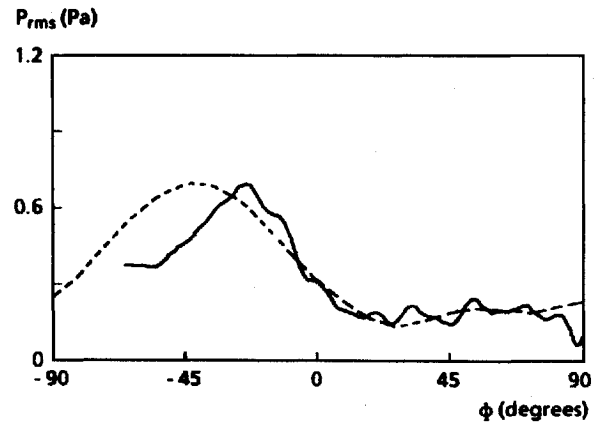

Fig. 11 Far-field directivity pattern in the θ = 90-deg plane, f = 1.5 kHz, azimuthal mode m = 1: - - - -, computation and ——, experiment.

Figure 15 shows that, at 1.5 kHz, for $m = 2$, the radiated field is more directional for the experimental result than for the computations. The same explanations apply as for results in the $\theta = 90$-deg plane (Fig. 12).

Pressure Field in the Duct Exit Plane

The data now presented are the pressure field, computed using the BIM on a disk close to the duct exit. Figure 16 presents contour plots of the pressure field. The SPL corresponds to an arbitrary modal amplitude of 1 on the source disk [i.e., $A = 1$ in Eq. (3)].

Figure 16a shows the pressure field for the $m = 0$ source configuration, at $f = 1$ kHz. The radiation pattern is symmetrical with

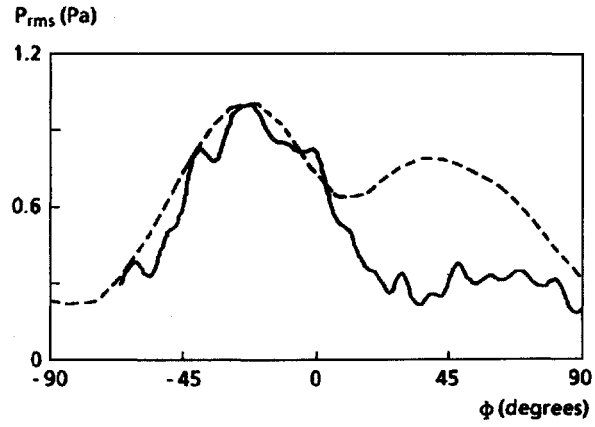

Fig. 12 Far-field directivity pattern in the θ = 90-deg plane, f = 1.5 kHz, azimuthal mode m = 2: - - - -, computation and ——, experiment.

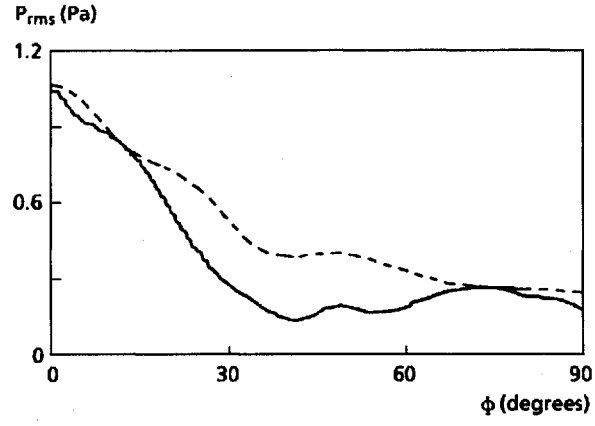

Fig. 13 Far-field directivity pattern in the θ = 0-deg plane, f = 1 kHz, azimuthal mode m = 0: - - - -, computation and ——, experiment.

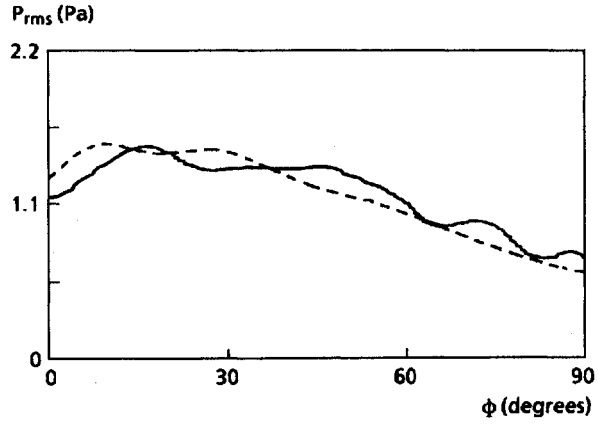

Fig. 14 Far-field directivity pattern in the θ = 0-deg plane, f = 1 kHz, azimuthal mode m = 1: - - - -, computation and ——, experiment.

respect to the xz plane (i.e., with respect to the geometric symmetry plane). This result is in agreement with the previous directivity pattern (Fig. 9), for this configuration. Only weak sound amplitude differences of about 4 dB are observed on the disk surface.

Figure 16b shows the pressure field for the $m = 1$ source configuration, at the same frequency, $f = 1$ kHz. Important SPL variations with a 30-dB range are now observed. The symmetry of the pressure field with respect to the xz plane is destroyed. This result is in agreement with the directivity pattern (see Fig. 10).

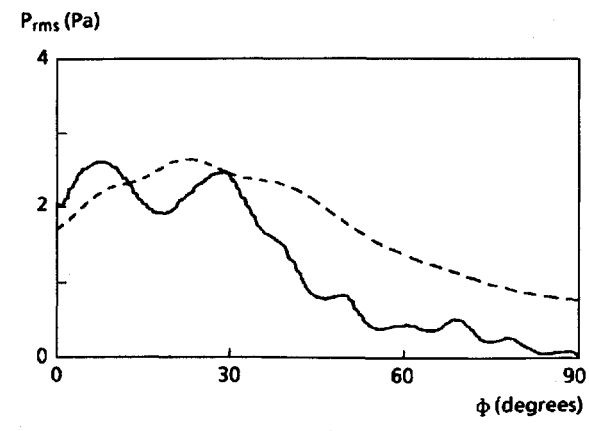

Fig. 15 Far-field directivity pattern in the θ = 0-deg plane, f = 1.5 kHz, azimuthal mode m = 2: - - - -, computation and ——, experiment.

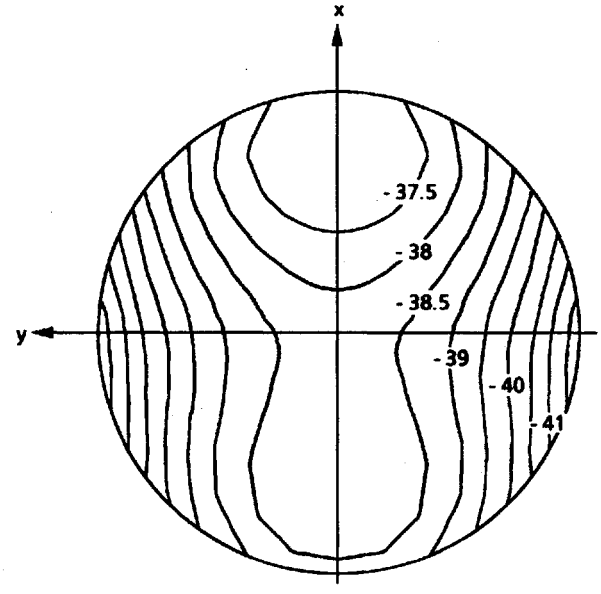

a) m = 0

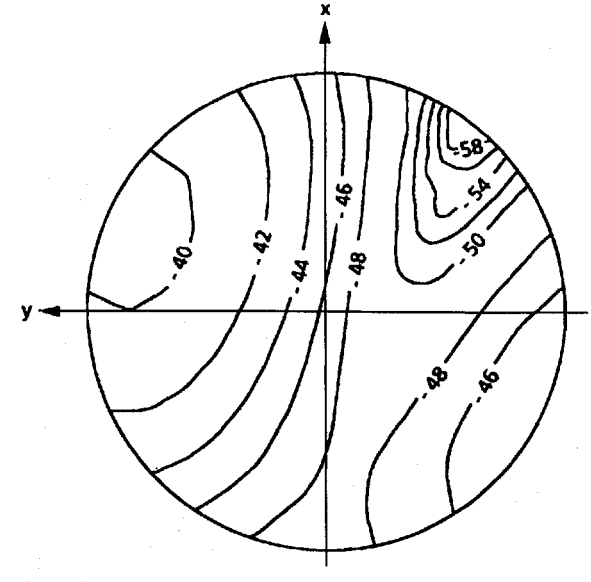

b) m = 1

Fig. 16 Pressure field in the duct exit plane, frequency f = 1 kHz.

VI. Summary

This paper illustrates an application of a BIM to propagation and radiation in a curved duct with a circular cross section. The comparison between numerical and experimental results shows the validity of the method in the midfrequency range for a plane wave mode, as well as for nonplane modes at the source. The incident mode at the source is redistributed by the bend toward all propagating modes. These modes detected at the curved exit are coherent and exhibit phase relationships. As a result of this phenomenon, for nonplane wave modes, the directivity patterns are not symmetrical with respect to the geometric symmetry plane of the duct.

For the $m = 2$, $f = 1.5$-kHz configuration, the agreement of the directivity patterns is not as good as in other configurations. This difference can be attributed to the source modeling. The authors suggest that more accurate results could be obtained using an adequate sound pressure distribution at the source location. In particular, it may be necessary to implement a method for separating the incident and reflected fields on the source surface S_1. The present model is indeed valid only if the pressure field reflected by the bend is negligible with respect to the incident field in the source vicinity. Such an improvement would provide a very powerful tool for predicting radiation by realistic turbomachinery inlets.

Acknowledgments

This work was supported by the Direction de la Recherche et de la Technologie. The authors would like to thank S. Lévy for his fruitful cooperation, as well as C. Polacsek and H. Gounet for providing the experimental results.

References

[1]Tyler, J. M., and Sofrin, T. G., "Axial Flow Compressor Noise Studies," *Transactions of the Society of Automotive Engineers*, Vol. 70, 1962, pp. 309–332.

[2]Baumeister, K. J., "Time-Dependent Difference Theory for Noise Propagation in a Two-Dimensional Duct," *AIAA Journal*, Vol. 18, No. 12, 1980, pp. 1470–1476.

[3]Baumeister, K. J., "Influence of Exit Impedance on Finite Difference Solutions of Transient Acoustic Mode Propagation in Ducts," *Journal of Engineering for Industry*, Vol. 104, Feb. 1982, pp. 113–120.

[4]Cabelli, A., "Duct Acoustics—A Time Dependent Difference Approach for Steady State Solutions," *Journal of Sound and Vibration*, Vol. 85, No. 3, 1982, pp. 423–434.

[5]Roy, I. D., and Eversman, W., "Improved Finite Element Modeling of the Turbofan Engine Inlet Radiation Problem," *Journal of Vibration and Acoustics*, Vol. 117, Jan. 1995, pp. 109–115.

[6]Kempton, A. J., "Ray Theory to Predict the Propagation of Broadband Fan-noise," AIAA Paper 80-0968, June 1980.

[7]Kempton, A. J., and Smith, M. G., "Ray Theory Predictions of the Sound Radiated from Realistic Engine Intakes," AIAA Paper 81-1982, Oct. 1981.

[8]Boyd, W. K., Kempton, A. J., and Morfey, C. L., "Ray Theory Predictions of the Noise Radiated from Aeroengine Ducts," AIAA Paper 84-3223, Oct. 1984.

[9]Hamdi, M. A., "Formulation Variationnelle par Equations Intégrales pour le Calcul de Champs Acoustiques Linéaires Proches et Lointains," Doctoral Thesis, Mechanics Dept., Université de Compiègne, France, June 1982.

[10]Malbéqui, P., Candel, S. M., and Rignot, E., "Boundary Integral Calculations of Scattered Fields: Application to a Spacecraft Launcher," *Journal of the Acoustical Society of America*, Vol. 82, No. 5, 1987, pp. 1771–1781.

[11]Elias, G., and Malbéqui, P., "Scattering by an Open Sphere: Exact Solution and Comparison with a Boundary Integral Method," *Journal of the Acoustical Society of America*, Vol. 93, No. 2, 1993, pp. 609–616.

[12]Lévy S., "Exact and Simplified Computation of Noise Radiation by an Annular Duct," *Proceedings of Inter-Noise 88*, Vol. 3, Noise Control Foundation, New York, 1988, pp. 1559–1564.

[13]Hamdi, M. A., and Ville, J. M., "Sound Radiation from Ducts: Theory and Experiment," *Journal of Sound and Vibration*, Vol. 107, No. 2, pp. 231–242.

[14]Malbéqui, P., and Candel, S. M., "Analyse de problèmes de diffraction par une méthode d'équation intégrale," ONERA TR 12/3571 PN, Jan. 1985.

[15]Wang, K. S., and Tszeng, T. C., "Propagation and Radiation of Sound in a Finite Length Duct," *Journal of Sound and Vibration*, Vol. 93, No. 1, 1984, pp. 57–79.

[16]Mébarek, L., and Hamdi, M. A., "Résolution du Problème des Fréquences Irrégulières en Equations Intégrales," 10th Colloque d'Acoustique Aéronautique et Navale, Marseille, France, Nov. 19–21, 1986.

[17]Polacsek, C., "Basic Experiments on the Directivity of a Turboshaft Engine Acoustic Radiation," 2nd French Conf. on Acoustics, *Journal de Physique IV*, Vol. 2, April 1992, pp. C1.611–C1.614.

[18]Blacodon, D., and Lévy, S., "Spinning Mode Analysis of the Acoustic Field Generated by a Turboshaft Engine," *Journal of Aircraft*, Vol. 29, No. 6, 1992, pp. 1073–1079.

[19]Lévy, S., "High-Frequency Acoustic Radiation from a Curved Duct of Circular Cross Section," *Proceedings of Noise-Con 93*, Vol. 1, Noise Control Foundation, New York, 1993, pp. 117–122.